

MESA Isochrones and Stellar Tracks (MIST) II. Models with α -enhanced chemical composition

AARON DOTTER,¹ EVAN B. BAUER,² MINJUNG PARK,² CHARLIE CONROY,² ANTONINO P. MILONE,^{3,4} MERIDITH JOYCE,⁵
AND MATTEO CANTIELLO^{6,7}

¹*Department of Physics and Astronomy, Dartmouth College, 6127 Wilder Laboratory, Hanover, NH 03755, USA*

²*Center for Astrophysics | Harvard & Smithsonian, 60 Garden Street, Cambridge, MA 02138, USA*

³*Dipartimento di Fisica e Astronomia “Galileo Galilei”, Università di Padova, Vicolo dell’Osservatorio 3, Padova 35122, Italy*

⁴*Istituto Nazionale di Astrofisica – Osservatorio Astronomico di Padova, Vicolo dell’Osservatorio 5, Padova 35122, Italy*

⁵*University of Wyoming, 1000 E University Ave, Laramie, WY USA*

⁶*Center for Computational Astrophysics, Flatiron Institute, New York, NY 10010, USA*

⁷*Department of Astrophysical Sciences, Princeton University, Princeton, NJ 08544, USA*

(Accepted)

Submitted to ApJS

ABSTRACT

We update and expand the MESA Isochrones and Stellar Tracks (MIST) database to include variations in the α -capture elements, specifically $[\alpha/\text{Fe}] = -0.2, 0, +0.2, +0.4, \text{ and } +0.6$ for $-3 \leq [\text{Fe}/\text{H}] \leq +0.5$. Variations in $[\alpha/\text{Fe}]$ are included in a self-consistent manner from the stellar interior models to the synthetic spectra used to translate these models in the observational plane. We describe a number of updates to the physics utilized in these models as well as new information provided by the models. We validate the models with comparisons to other stellar evolution models including the previous generation of MIST and other models from the literature. MIST data products including stellar evolution tracks, isochrones, and bolometric correction tables can be obtained from the MIST project website, <https://mist.science>. All necessary files to reproduce MIST models are available from Zenodo.

1. INTRODUCTION

Stellar models form the backbone of many areas of astrophysics, from the interpretation of the highest redshift galaxies to the determination of exoplanet masses and radii. These models have been under a constant state of development since computer programs were designed to solve the equations of stellar structure in the early 1950s (Oke & Schwarzschild 1952). Modern research efforts involve computing the evolution of large grids of stars from the an initial condition through advanced phases of stellar evolution, including heavy-element nucleosynthesis for massive stars and through thermal pulses during the asymptotic giant branch (AGB) phase for lower-mass stars (e.g., Marigo et al. 2013; Choi et al. 2016; Marigo et al. 2017; Joyce et al. 2024).

To be maximally useful, grids of stellar models are expected to cover a wide range in age, evolutionary phase, initial mass, and initial $[\text{Fe}/\text{H}]$. In the case of $[\text{Fe}/\text{H}]$, it is sometimes assumed that the relative abundance ratios of individual elements is fixed to the adopted solar mixture so that one single parameter, the mass fraction of all metals (Z), determines the overall element abundance pattern. However, it is well known that stars and stellar systems exhibit abundance patterns that deviate substantially from the (scaled) solar mixture. This is expected because different sites for nucleosynthetic enrichment — core-collapse supernovae, thermonuclear detonation of white dwarfs, shell-burning in AGB stars — produce different abundance patterns (Clayton 1984). The most common observed deviation from the solar mixture is a change in the α -capture elements (O, Ne, Mg, Si, S, Ar, Ca, Ti) with respect to the Fe-peak elements. This deviation is often parameterized as $[\alpha/\text{Fe}]$, the ratio of α -capture elements compared to Fe elements relative to the solar ratio. Note that the term “ α -enhanced” is used loosely to refer to models within which $[\alpha/\text{Fe}] \neq 0$.

Stars and stellar systems that display non-scaled-solar abundance patterns are ubiquitous. In the Milky Way, the majority of stars with $[\text{Fe}/\text{H}] < -1$ are α -enhanced (Tolstoy et al. 2009), as are nearly all globular clusters (Pritzl et al. 2005). Populations with non-solar abundance patterns are common among dwarf galaxies in the Local Group,

arXiv:2602.22012v1 [astro-ph.SR] 25 Feb 2026

as well as the most massive galaxies in the universe (Worthey et al. 1992; Worthey 1994; Trager et al. 2000; Conroy 2013). There is even evidence that massive star-forming galaxies at $z \sim 2$ harbor α -enhanced stellar populations (e.g., Bensby et al. 2014; Steidel et al. 2016; Cullen et al. 2019; Topping et al. 2020; Kashino et al. 2022).

These facts motivate the need for large grids of stellar evolution models that span a range in $[\alpha/\text{Fe}]$ as well as $[\text{Fe}/\text{H}]$. Recent grids of α -enhanced stellar models have mostly focused on the lower masses and older ages relevant for globular clusters (e.g., Dotter et al. 2008; VandenBerg et al. 2014; Fu et al. 2018). Recent grids covering a wider range in masses and ages include BaSTI (Hidalgo et al. 2018; Pietrinferni et al. 2021) and PaRSEC (Bressan et al. 2012; Chen et al. 2014; Nguyen et al. 2022). Few, if any, previous models exist that span the full range in masses (e.g., $0.1 - 100M_{\odot}$), metallicities including both $[\text{Fe}/\text{H}]$ and $[\alpha/\text{Fe}]$, and evolutionary phases. The main purpose of this paper is to provide such an expansive grid.

A breakthrough in stellar evolution modeling has occurred over the past 15 years thanks to the Modules for Experiments in Stellar Astrophysics (MESA) software instrument (Paxton et al. 2011, 2013, 2015, 2018, 2019; Jermyn et al. 2023). In previous work we employed MESA to build a comprehensive grid of stellar evolution tracks and isochrones, referred to as MESA Isochrones and Stellar Tracks (MIST) (Dotter 2016a; Choi et al. 2016, hereafter Papers 0 and 1, respectively). These models evolved stars with masses from $0.1 - 300M_{\odot}$ from pre-main sequence contraction through either central carbon burning or white dwarf cooling, depending on the initial mass, and cover scaled-solar compositions from $[\text{Fe}/\text{H}] = -3$ to $+0.5$.

In this work we update the MIST database in two important respects. First, we describe updates to the stellar physics. Second, we expand the coverage beyond solar-scaled compositions to include a range of α -enhancements from $[\alpha/\text{Fe}] = -0.2$ to $+0.6$ in steps of 0.2 dex. These new models are available for download from the MIST project webpage¹ and Zenodo.

2. THE MIST STELLAR MODELS

Paper 1 gives a detailed description of the adopted physics, notably including mixing processes, rotation, and mass loss, used in the MESA models that form the foundation of MIST, as well as information about how those tracks are converted into isochrones (see also Paper 0), and how both types of models are transformed into the observational plane.

In this paper, the algorithmic treatment of microphysics (equation of state [EOS] and opacities), nucleosynthesis, mixing, rotation, and mass loss are essentially the same as described in Paper 1, except where we describe extensions of the microphysics in the subsections below. We therefore do not exhaustively revisit all microphysics inputs in detail; the reader is referred to Paper 1 for topics not covered here, as well as to the repository of codes shared with this paper that enable full reproduction of all stellar modeling (see Section 2.2).

2.1. Abundances

We use the term $[\alpha/\text{Fe}]$ to be representative of the α -capture elements. It is not possible to express a single definition of “ α -enhancement” that works for all stars in all environments. Instead, stellar models of α -enhanced stars have chosen a number of different patterns. In the past, a variety of different α -enhancement patterns were used to compute stellar evolution models, notably the mixture adopted by Salaris & Weiss (1998) that was used in previous generations of the Padova (Salasnich et al. 2000) and BaSTI models (Pietrinferni et al. 2006). However, the latest grids from Victoria-Regina VandenBerg et al. (2014), BaSTI (Pietrinferni et al. 2021), and Dartmouth (Dotter et al. 2008) adopt an approach where each α -element is enhanced by the same amount relative to its scaled-solar abundance, and that value is equal to $[\alpha/\text{Fe}]$. This fixed approach is adopted in the present work as well.

It is worthwhile to note that while the α -enhancement pattern used by Dartmouth, Victoria-Regina, and BaSTI is the same as in this work, the adopted solar abundance patterns differ: Dartmouth used Grevesse & Sauval (1998, hereafter GS98), BaSTI used Caffau et al. (2011), and Victoria-Regina adopted the Asplund et al. (2009) solar mixture. While Paper 1 adopted the Asplund et al. (2009) solar abundances, we have instead adopted Grevesse & Sauval (1998) in this paper for two reasons: first, the latest analyses of the solar abundances are tending back towards solar metal abundances consistent with GS98 (Magg et al. 2022; Pietrow et al. 2023) and, second, there are high- and low-temperature opacities readily available for the GS98 composition with α -element enhancements.

¹ <http://mist.science>

The MIST model grids include 15 $[\text{Fe}/\text{H}]$ values spanning $-3 \leq [\text{Fe}/\text{H}] \leq +0.5$ and 5 $[\alpha/\text{Fe}]$ values spanning $-0.2 \leq [\alpha/\text{Fe}] \leq +0.6$ for a total of 74 unique chemical compositions. The grid spacing is 0.2 dex in $[\alpha/\text{Fe}]$ and 0.25 dex in $[\text{Fe}/\text{H}]$, except for $[\text{Fe}/\text{H}] < -3$ where the spacing is 0.5. We exclude the grid at $[\text{Fe}/\text{H}] = +0.5$, $[\alpha/\text{Fe}] = +0.6$ due to the lack of necessary input physics.

In the following, we relate the mass fraction of helium (Y) and all heavier elements (Z) used in our models. The helium enrichment with respect to heavier elements, $\Delta Y/\Delta Z$, expressed as

$$\frac{\Delta Y}{\Delta Z} = \frac{Y_{\odot, \text{init}} - Y_p}{Z_{\odot, \text{init}} - 0} = \frac{0.0245}{0.0185} \approx 1.32 \quad (1)$$

where the subscript p refers to the primordial value derived from Big Bang Nucleosynthesis ($Y_p = 0.249$, [Planck Collaboration et al. 2015](#)) and the \odot, init symbol refers to the initial value of our solar-calibrated model (see Table 1). This value is lower than that used in Paper 1 ($\Delta Y/\Delta Z=1.5$) because of the chosen proto-solar abundances (see Section 1 and Table 4 of Paper 1).

2.2. MESA

For the present work we use the MESA software instrument ([Paxton et al. 2011, 2013, 2015, 2019; Jermyn et al. 2023](#)) version 11701 ([Paxton 2019](#)) supported by the MESA SDK ([Townsend 2019](#)). We use radiative opacities from OPAL [Iglesias & Rogers \(1996\)](#) and [Ferguson et al. \(2005\)](#); nuclear reaction rates from JINA REACLIB ([Cyburt et al. 2010](#)); the EOS is a combination of OPAL ([Rogers & Nayfonov 2002](#)), SCvH ([Saumon et al. 1995](#)), HELM ([Timmes & Swesty 2000](#)), and PC ([Potekhin & Chabrier 2010](#)) as detailed in [Paxton et al. \(2011, 2019\)](#). We have utilized EOS tables computed with the FreeEOS² software instrument to supplement the partially-ionized parameter space otherwise covered by the OPAL EOS for metal mass fraction $Z \geq 0.04$. The FreeEOS tables were provided for later versions of MESA as described by [Jermyn et al. \(2023\)](#) and backported into MESA version 11701. The version of MESA used in this paper was modified to fix a couple of issues that were discovered in newer versions of MESA as well as support for the aforementioned FreeEOS tables, atmosphere boundary condition tables, and extended sets of Rosseland mean opacity tables to properly reflect the $[\alpha/\text{Fe}]$ variations covered by the MIST model grid. (All references to opacity in this paper refer to the Rosseland mean opacity.) In order to enable reproducibility of all our stellar modeling, we make available our entire MESA installation including modifications ([Dotter & Bauer 2025a](#)) as well as work directories, inlists, and all other input files ([Dotter & Bauer 2025b](#)). An elucidation of the changes made is given in the Appendix.

The impact of $[\alpha/\text{Fe}]$ variations on stellar structure can enter our models through multiple aspects of the microphysics, including the opacities, EOS, atmosphere boundary conditions, and nuclear reactions. The treatment of nuclear reaction networks in MESA accounts for the full composition vector of the model, so nuclear reactions will naturally incorporate the impact of $[\alpha/\text{Fe}]$ variations, but the treatments for other aspects of microphysics mentioned above all contain components that rely on interpolating tables that by default assume solar-scaled metallicity mixtures. We therefore supplement the default treatments for tabulated opacities and atmosphere boundary conditions with additional tabulations to capture $[\alpha/\text{Fe}]$ variations. For opacities, we used additional OPAL opacity tables for each of the 5 $[\alpha/\text{Fe}]$ values covered by our model grids, using the GS98 abundance mixture with α -capture elements scaled as described in Section 2.1. For atmosphere boundary condition tables, we describe our supplemental treatment in Section 2.3. The low-temperature opacities and the atmosphere boundary conditions are responsible for mediating by far the largest impact of composition variations on our stellar interior models ([Weiss et al. 2006; Dotter et al. 2007a; VandenBerg et al. 2012](#)).

2.3. The Atmosphere Boundary Condition

As in Paper 1, we use a hybrid approach to setting the atmosphere boundary condition in our stellar evolution models. For stellar models with $M \geq 8M_{\odot}$, we use the `simple_photosphere` option in MESA—this amounts to the (simple) assumption that the opacity in the atmosphere is a constant that can be pulled out of the T - τ integration.

For stellar models with $M < 8M_{\odot}$, we use the T - τ integration method described by [Dotter \(2022\)](#). The T - τ relation refers to a relation between temperature (T) and Rosseland mean optical depth (τ) in the stellar atmosphere. The T - τ relation from [Vernazza et al. \(1981\)](#) is adopted. The method extends the atmosphere boundary condition T - τ integration by checking the local conditions for convection at each step in the numerical integration and substituting

² <https://freeeos.sourceforge.net/documentation.html>

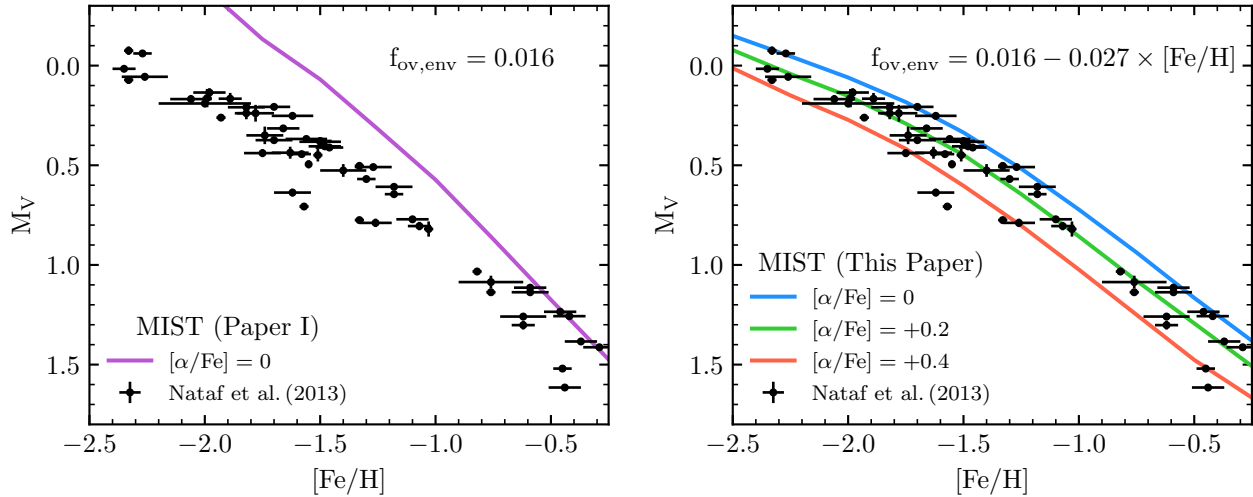


Figure 1. The Red Giant Branch Bump (RGBB) data sample compiled by [Nataf et al. \(2013\)](#) is compared with Paper 1 (left) and this paper (right) at 12 Gyr. Paper 1 models have only scaled-solar composition. The main difference between the two panels is the calibration of $f_{\text{ov,env}}$ (see Section 2.5 for details).

the values derived from the mixing length theory (MLT) when convection is present. This method enables the matching point between the atmosphere integration and the interior model to be safely made at a point where the model is convective. As pointed out by [Chabrier & Baraffe \(1997\)](#) there is considerable advantage to choosing the match point between atmosphere and interior within the surface convection zone (if there is one). The fitting point between atmosphere integration and interior model is chosen to be $\tau = 10$, which is confirmed to be within the surface convection zone for all models that have a convective surface layer. The T - τ integrations are tabulated according to surface T_{eff} and $\log(g)$, analogous to the way that model atmosphere boundary condition tables are structured. Individual tables are made for each of the distinct chemical compositions in this paper. These tables are used within MESA in place of the default set of tabulated atmosphere boundary conditions.

2.4. Rotation

As in Paper 1, we include two sets of models: one with and one without rotation. Models with rotation are initialized with angular velocity $\Omega = 0.4\Omega_{\text{crit}}$ near the Zero Age Main Sequence (ZAMS) for $M_{\text{init}} \geq 1.8M_{\odot}$, with rotation ramped³ down to zero for models with $M_{\text{init}} \leq 1.2M_{\odot}$. Here Ω_{crit} is the critical (Keplerian) angular velocity. Modeling of rotation includes both angular momentum transport and associated compositional mixing with a relative efficiency factor of $f_c = 1/30$ for compositional diffusivity relative to angular momentum diffusivity ([Paxton et al. 2013](#), section 6). The rotational mixing processes accounted for include dynamical shear instability, secular shear instability, Solberg-Høiland (SH) instability, Eddington-Sweet (ES) circulation, and Goldreich-Schubert-Fricke (GSF) instability ([Pinsonneault et al. 1989](#); [Heger et al. 2000](#); [Paxton et al. 2013](#)).

In addition to these rotational processes that were included in Paper 1, the model grids now also include angular momentum transport due to the Tayler-Spruit mixing ([Spruit 2002](#)) following the prescription of [Fuller et al. \(2019\)](#). This additional angular momentum transport allows compact cores to spin down on the red giant branch (RGB) and asymptotic giant branch (AGB) and achieves reasonable agreement with seismologically-inferred spin rates of cores on the RGB and red clump ([Mosser et al. 2012](#); [Deheuvels et al. 2015](#); [Gehan et al. 2018](#)). Because this prescription is primarily calibrated for intermediate mass stars and their white dwarf descendants, we only apply this [Fuller et al. \(2019\)](#) prescription for models with $M < 7M_{\odot}$, with the mechanism fully on for $M < 4M_{\odot}$ and ramped down to zero for $4M_{\odot} < M < 7M_{\odot}$. By the time these models reach the end of the AGB, their cores have slowed sufficiently to evolve into white dwarfs that will generally agree with observed \sim day spin periods for white dwarfs ([Hermes et al. 2017](#); [Fuller et al. 2019](#)).

³ The ‘ramp’ function mentioned here and in the following paragraph is sinusoidal, rather than linear, in nature. The purpose of this is to affect the ramp without introducing a discontinuity in the first derivative.

2.5. *Mixing Processes*

We use the exponential-decay formalism (Herwig 2000, equation 2), with adjustable parameter f , to model mixing across radiative-convective boundaries. Overshoot mixing was calibrated in Paper 1, adopting the same parameter f_{ov} for all mixing boundaries. It should be noted that the calibration of overshoot parameters performed in Paper 1 was done using the solar calibration. The need to perform an additional calibration was motivated by the inability of MIST models to correctly predict the observed trend in the brightness of the red giant branch bump (RGBB), the overdensity of stars created when the H-burning shell briefly meets the bottom of the surface convection zone during red giant evolution, with metallicity (see Figure 1).

Using the data set compiled by Nataf et al. (2013), we have undertaken to calibrate the overshoot parameter specifically for the case of mixing below the surface convection zone, $f_{\text{ov,env}}$. The procedure involved computing sets of stellar models with our standard configuration while varying only $f_{\text{ov,env}}$ at a range of metallicities corresponding to the Nataf et al. (2013) dataset. With these sets of models computed, it was possible to a relation between $f_{\text{ov,env}}$ and $[\text{Fe}/\text{H}]$ that follows the trend seen in the data,

$$f_{\text{ov,env}} = 0.016 - 0.027 \times [\text{Fe}/\text{H}] \quad (2)$$

with the further constraint that $0.01 \leq f_{\text{ov,env}} \leq 0.08$ because of the limited $[\text{Fe}/\text{H}]$ range of the Nataf et al. (2013) sample compared to the $[\text{Fe}/\text{H}]$ range of the models. The value of $f_{\text{ov,env}} = 0.016$ is the solar-calibrated value from Paper 1.

Figure 1 demonstrates the result of the $f_{\text{ov,env}}$ calibration. The left panel shows the trend with $[\text{Fe}/\text{H}]$ for Paper 1 models and the right panel shows the trends from this paper, including a range of α -enhancement. The result of the calibration described here is that the models follow the observed trend over the full range of $[\text{Fe}/\text{H}]$, whereas the uncalibrated models from Paper 1 predicted a much steeper trend, with the bump magnitude being over-predicted by roughly 0.5 for the most metal-poor globular clusters.

Paper 1 implemented the ‘radiation turbulence’ model (Morel & Thévenin 2002) to inhibit atomic diffusion near the stellar surface. In this paper the surface mixing has been changed to the turbulent diffusion treatment described by VandenBerg et al. (2012); for discussion see Section 2.1 of Dotter et al. (2017).

2.6. *Solar Calibration*

The changes with respect to Paper 1 summarized above, especially the change of solar abundance pattern, necessitated a revised solar calibration. We adopt the nominal solar values of IAU Resolution 2015.B3 (Prša et al. 2016). The results of the solar calibration and the initial parameters of the solar model are summarized in Table 1.

2.7. *Evolutionary Coverage*

Paper 1 described evolutionary models that covered from the pre-main sequence to either the end of the main sequence (for very-low-mass stars), to the white dwarf cooling sequence (for low- and intermediate-mass stars), or to the end of central C-burning (for high-mass stars). In this paper evolutionary coverage is the same for very-low-mass and high-mass stars. However, for low- and intermediate-mass stars we have stopped the evolution once the models reach the end of the thermally-pulsating asymptotic giant branch (TP-AGB) phase, having shed the majority of the H-rich envelope and begun to evolve to higher T_{eff} .

Significant improvements to the treatment of white dwarf models in MESA versions subsequent to MESA 11701 motivate a separate study dedicated to extending the current evolutionary tracks onto the white dwarf cooling curve (Bauer 2023; Jermyn et al. 2023). The low and intermediate mass models therefore end at the post-AGB phase with their core composition largely set, ready to evolve over to and down the cooling sequence as white dwarfs. Updated white dwarf cooling models in the MIST framework is described in a companion paper (Bauer et al., accepted to ApJ).

2.8. *Evolutionary Tracks and Isochrones*

Evolutionary tracks and isochrones are constructed using the ‘equivalent evolutionary phase’ (EEP) formalism and the `iso` code (Dotter 2016b), described in Paper 0. Stellar evolution tracks computed by MESA are converted into EEP-based tracks and then those EEP-based tracks are interpolated into isochrones. Tracks and isochrones provided on the MIST project webpage use the same file format as in Paper 1. Some additional data columns have been added, as described in Section 2.5. The file format is otherwise unchanged from Paper 1.

Table 1. Solar calibration results for MIST2

Parameter	Target	Model Value
$\log(L/L_{\odot})$	0	3.72×10^{-6}
$\log(R/R_{\odot})$	0	-5.33×10^{-5}
Y_{surf}	0.2485 ^a	0.2482
$[\text{Fe}/\text{H}]_{\text{surf}}$	0 ^b	0.003
R_{cz}/R_{\odot}	0.7133 ^c	0.7174
α_{MLT}	...	2.03
$f_{\text{ov, env}}$...	0.016
X_{initial}	...	0.7080
Y_{initial}	...	0.2735
Z_{initial}	...	0.0185

NOTE—The top half compares observed and modeled values at the solar age. The bottom half lists solar-calibrated model parameters. X , Y , and Z refer to the mass fractions of hydrogen, helium, and all heavier elements, respectively. Subscript ‘surf’ refers to the surface value of the model. Subscript ‘cz’ refers to the location of the bottom of the surface convection zone. α_{MLT} is the mixing length parameter and $f_{\text{ov, env}}$ is described section 2.5.

^a Basu et al. (2004)

^b GS98

^c Basu et al. (2004)

2.9. Synthetic Spectra and Bolometric Corrections

Our stellar evolution tracks and isochrones specify physical properties (T_{eff} , $\log(g)$, composition) at the surface, which must then be transformed into observables through synthetic spectra and bolometric corrections for a variety of filter sets. We accomplish this with a custom grid of stellar spectral models calculated using the 1D LTE plane-parallel atmosphere and radiative transfer codes ATLAS12 and SYNTHE maintained by R. Kurucz (Kurucz 1970; Kurucz & Avrett 1981; Kurucz 1993, 2011). The line list used in the radiative transfer calculation was provided by R. Kurucz and has been empirically tuned to the observed, ultra-high-resolution spectra of the Sun and Arcturus, including the ExoMol TiO database from McKemmish et al. (2019). We adopt a constant microturbulence of $v_{\text{micro}} = 1 \text{ km s}^{-1}$. The grid is computed with $\Delta \log g = 0.5$ over the range $[-1, 5]$, $\Delta [\text{Fe}/\text{H}] = 0.25$ over the range $[-3, +0.5]$, $\Delta [\alpha/\text{Fe}] = 0.2$ over the range $[-0.2, +0.6]$, and an irregular (approximately log-spaced) T_{eff} grid with 40 points between 3500 and 15,000 K. We compute synthetic spectra at a resolving power of $R = 1,000,000$, and then subsequently smooth to a resolution of $R = 42,000$. The abundance patterns used in the stellar atmospheres and interior models are identical, as much as possible, considering that the model atmospheres and synthetic spectra include abundances of many more elements than are directly modeled by the stellar interior code.

We adopt the IAU resolution 2015.B2 (Mamajek et al. 2015) recommended value for the zeropoint of the bolometric magnitude scale, in which the adopted nominal solar luminosity corresponds to an absolute bolometric magnitude for the sun of $M_{\text{Bol}, \odot} = 4.74$. Bolometric corrections are constructed following Girardi et al. (2008); the integrals are evaluated in ‘photon counting’ mode, not energy counting (Bessell & Murphy 2012). Zeropoints defining the photometric standard system are chosen individually for each filter set from one of either Vega (Bohlin 2016), AB (Oke 1974), or ST (Koornneef et al. 1986). In all regards this approach is identical to Paper 1. Extinction is incorporated inside the integral over wavelength for each filter and each synthetic spectrum. For this paper we have included the extinction curve derived by (Fitzpatrick & Massa 2007) with selective extinction $R_V = 3.1$ as well as a range of extinction A_V from 0 to 6. An up-to-date list of supported photometric systems is provided on the MIST webpage.

2.10. *New features*

A few new data columns have been added to the stellar evolution tracks and isochrones. A README file including descriptions of all table columns is provided on the MIST webpage. The following is a description of new columns added since Paper 1.

2.10.1. *Gravity darkening*

Paxton et al. (2019) introduced the capability to include the effects of gravity darkening in MESA rotating stellar evolution models via the theoretical framework of Espinosa Lara & Rieutord (2011). MIST stellar evolution tracks and isochrones have been expanded to include the luminosity and effective temperature that would be observed if the star were observed pole-on and equator-on in rotating models⁴. This information can be useful, for example, in estimating the envelope of possible observables for a given rotating stellar model depending on the orientation of the star’s spin axis with respect to the observer.

2.10.2. *Surface convection zone*

For stars with a surface convection zone, the tracks and isochrones include both the mass and radius coordinate of both the top and the bottom of zone. In addition, we provide estimates of the convective turnover time of the surface convection zone. One estimate is a global average, calculated as $\int \frac{dr}{v_{\text{conv}}}$ with r the radial coordinate and v_{conv} the convective velocity; the integral is over the radial extent of the surface convection zone. The other two estimates are local, and are given by the ratio of the mixing length ($\Lambda = \alpha_{\text{MLT}} H_P$) to the convective velocity evaluated locally at one half and one mixing length above the bottom of the surface convection zone.

2.10.3. *Internal structure*

A measure of central concentration, the apsidal motion constant k_2 (Kopal 1978) can also be measured directly from binary systems and, thus, constitutes a useful probe of stellar models.

3. BEHAVIOR OF THE MODELS

In this section, we present an overview of the isochrones on Hertzsprung-Russell (HR) diagrams and color-magnitude diagrams (CMDs), with an emphasis on the impact of the additional $[\alpha/\text{Fe}]$ dimension of the model grids compared to Paper I.

3.1. *New isochrones compared to Paper 1*

Figure 2 shows example isochrones at 10 Myr, 100 Myr, 1 Gyr, and 10 Gyr for two different values of $[\text{Fe}/\text{H}]$, at fixed $[\alpha/\text{Fe}] = 0$ for comparison to the solar-scaled isochrones from Paper 1. The only significant difference between versions that manifests in the H-R diagram in Figure 2 is the change of surface boundary condition and solar-calibrated α_{MLT} that influences the temperature scale of the RGB.

3.2. *Sensitivity of the models to $[\alpha/\text{Fe}]$*

As mentioned in Sections 2.1–2.3 and 2.9, the variations in the $[\alpha/\text{Fe}]$ dimension of composition impact both the physics of stellar evolution tracks and the bolometric corrections. Figure 3 shows two sets of isochrones at fixed $[\text{Fe}/\text{H}]$ displaying the full range of $[\alpha/\text{Fe}]$ in the H-R diagram. The influence of $[\alpha/\text{Fe}]$ is smaller at $[\text{Fe}/\text{H}] = -2.0$ than at $[\text{Fe}/\text{H}] = -0.5$. The overall effect is a combination of factors, including increasing (primarily) the oxygen abundance on the stellar lifetimes and modifying the opacity in the surface layers (see, e.g., Dotter et al. 2007b).

The possibility of reproducing the influence of α -enhancement on stellar evolution tracks and isochrones by (re)scaling the total Z of models with scaled-solar abundances has been discussed in the literature for years (Salaris et al. 1993). As already hinted at in Figure 2, the challenge becomes greater as total Z increases. Figure 4 shows two examples that demonstrate the value of having $[\alpha/\text{Fe}]$ and $[\text{Fe}/\text{H}]$ as independent dimensions. In each panel of Figure 4, α -enhanced isochrones are compared to two other isochrones at $[\alpha/\text{Fe}] = 0$, representing solar-scaled mixtures. One of these isochrones has the same value of $[\text{Fe}/\text{H}]$ while the other matches the total Z of the α -enhanced isochrone. While the case of $[\text{Fe}/\text{H}] = -0.5$ shown on the left panel of Figure 4 dictates that scaling total Z does an adequate job, the

⁴ These new columns are present in all data files but are not distinct for non-rotating models.

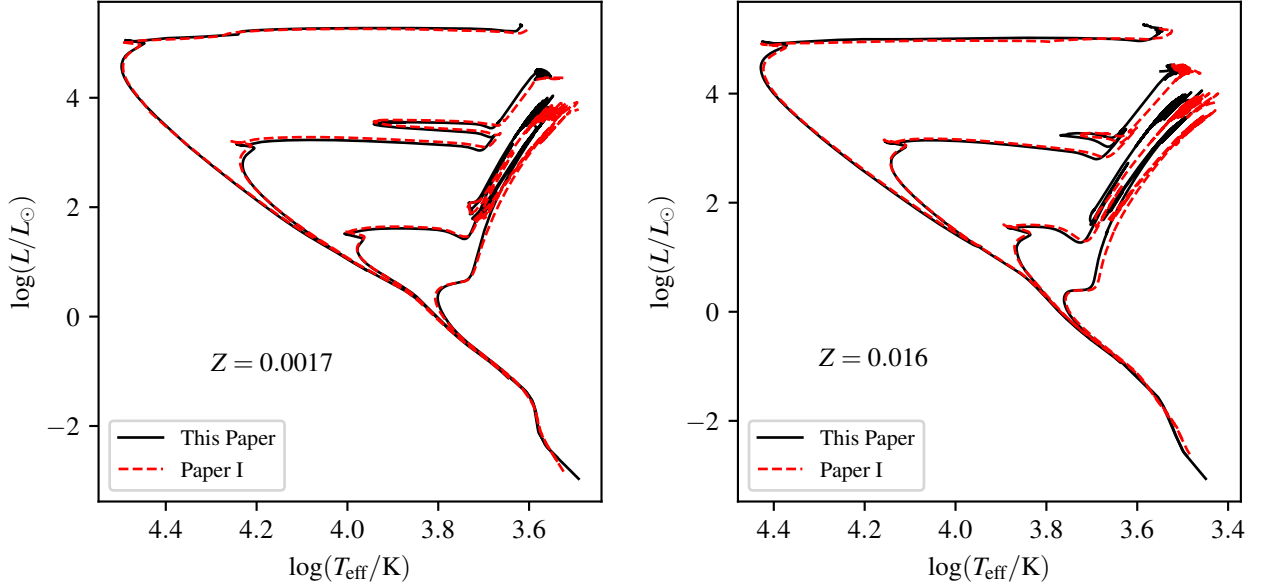


Figure 2. MIST isochrones at 10 Myr (upper left), 100 Myr, 1 Gyr, and 10 Gyr (lower right). The left panel shows $Z = 0.0017$ ($[\text{Fe}/\text{H}] \approx -1$) and the right panel shows $Z = 0.016$ ($[\text{Fe}/\text{H}] \approx 0$), for both Paper 1 (red) and this paper (black). In this and subsequent figures, the pre-MS evolution has been omitted from the younger ages for clarity.

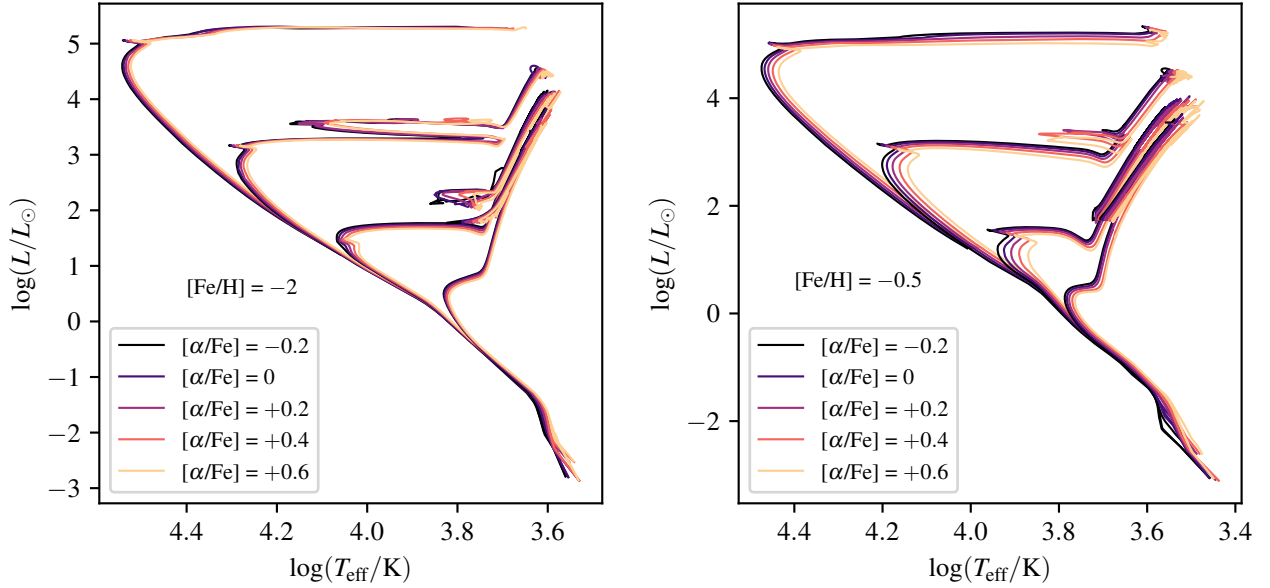


Figure 3. MIST isochrones at 10 Myr, 100 Myr, 1 Gyr, and 10 Gyr, showing the effect of $[\alpha/\text{Fe}]$ enhancements across the range -0.2 to $+0.6$ in the theoretical HR diagram. The left panel show $[\text{Fe}/\text{H}] = -2.0$ and the right panel shows $[\text{Fe}/\text{H}] = -0.5$ isochrones.

case shown on the left shows that the scaled-solar isochrones are not able to capture the morphologies of α -enhanced isochrones at older ages.

Figure 5 demonstrates the cumulative effects of α -enhancement on stellar models in the Hertzsprung-Russell diagram and the CMD. The HST/WFC3 photometric system is used because it spans the UV, optical, and near-infrared. Figure 5 shows the same isochrones with fixed age of 8 Gyr and fixed $[\text{Fe}/\text{H}] = -0.5$. Each row represents a different CMD from the UV (top), to the optical (middle), to the near-infrared (bottom). The models in the left column show the case

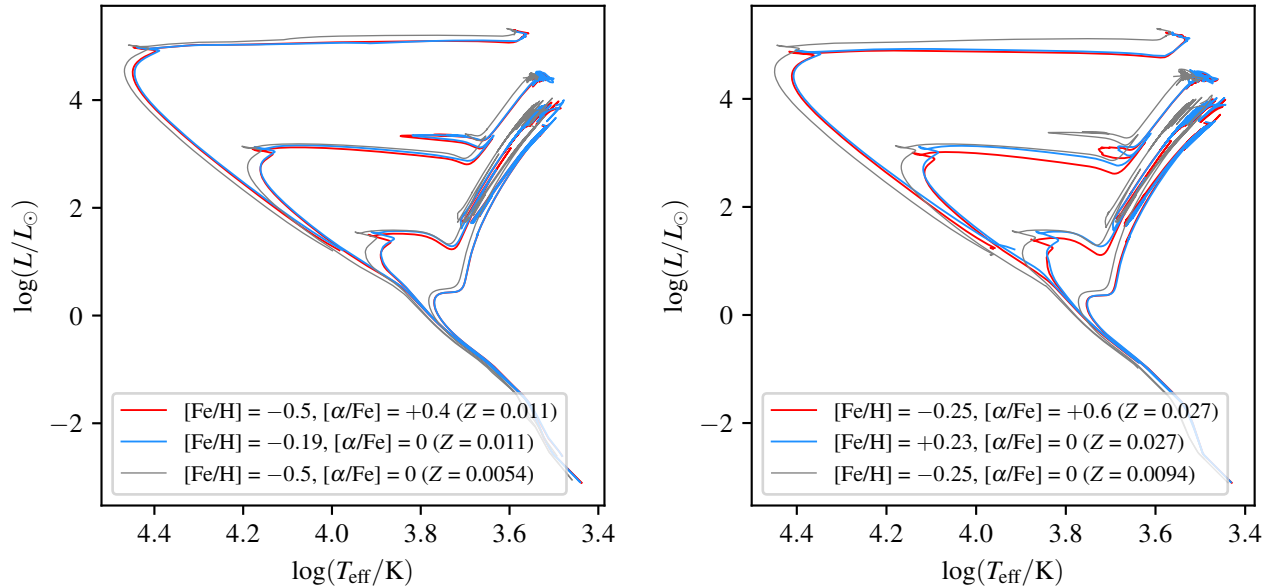


Figure 4. MIST isochrones at 10 Myr, 100 Myr, 1 Gyr, and 10 Gyr. The red line is the α -enhanced model with $[\text{Fe}/\text{H}] = -0.5$ (left) or -0.25 (right) while the blue line is made from a scaled-solar composition but interpolated to the same total Z as the red curve in each panel. For comparison, the gray lines are scaled-solar models with the same $[\text{Fe}/\text{H}]$ as the red lines.

where the underlying isochrone is kept fixed — in this case we use the isochrone with $[\alpha/\text{Fe}] = +0.2$ — and the level of α -enhancement varies from -0.2 to $+0.6$ only in the bolometric corrections, thereby isolating the spectral effect of α -enhancement. The middle column of Figure 5 shows the converse: in this case $[\alpha/\text{Fe}]$ varies in the underlying isochrones (as in Figure 3) but is kept fixed at $[\alpha/\text{Fe}] = +0.2$ in the bolometric corrections. The right column of Figure 5 shows the combined effects of α -enhancement on both the underlying isochrones and in the bolometric corrections.

The most dramatic effect in Figure 5 is seen below the “knee” in the CMD, where the effect of molecular absorption in the atmosphere becomes prominent. In this regime, the formation of molecules involving C, N, and O is modified by variations to the oxygen abundance via $[\alpha/\text{Fe}]$. In the near-infrared CMD, it is the formation of water molecules and the increased absorption primarily in the F160W filter. In the ultraviolet CMD, the oxygen competes with carbon and nitrogen for hydrogen atoms to a varying extent, depending on $[\alpha/\text{Fe}]$ (see Sbordone et al. 2011; Dotter et al. 2015). The variations seen in the optical CMD are less pronounced due to the lack of molecular lines in these filters.

3.3. Comparisons with other models

Figure 6 shows MIST α -enhanced isochrones (solid lines) compared to α -enhanced isochrones from BaSTI (dashed lines Pietrinferni et al. 2021) at the same $[\text{Fe}/\text{H}]$. Considering that Figure 6 is based on models coming from two different stellar evolution codes with differences in the adopted physics, the overall agreement is reassuring.

3.4. Comparisons with observations

In Figures 7 and 8 we compare MIST α -enhanced isochrones with CMDs of three Galactic globular clusters. These comparisons are not meant to be a detailed analysis of these clusters; we merely wish to demonstrate the capabilities of MIST. The isochrones were interpolated in $[\text{Fe}/\text{H}]$ from our grid. Evolution past the AGB is not included in either Figure 7 or 8 for clarity. We note that while globular clusters are representative of α -enhanced stellar populations, their stars also—and perhaps more importantly—contains variations in the light elements that are not consistent with α -enhancement (cf. Milone & Marino 2022).

The data shown in Figure 7 were taken from the ACS Survey of Galactic Globular Clusters (Sarajedini et al. 2007; Anderson et al. 2008) and we have chosen clusters spanning approximately 1.5 dex in $[\text{Fe}/\text{H}]$. Details of model parameters, distance moduli, and extinction parameters involved are provided in Table 2. The figures shows 4 isochrones in each panel, these are 10, 11, 12, and 13 Gyr, respectively, and all have $[\alpha/\text{Fe}] = +0.4$. Note that MIST isochrones include only a single value for RGB mass-loss and so will not describe a full zero-age horizontal branch sequence. Hence one should not expect to see full coverage of the horizontal branch stars in any CMD.

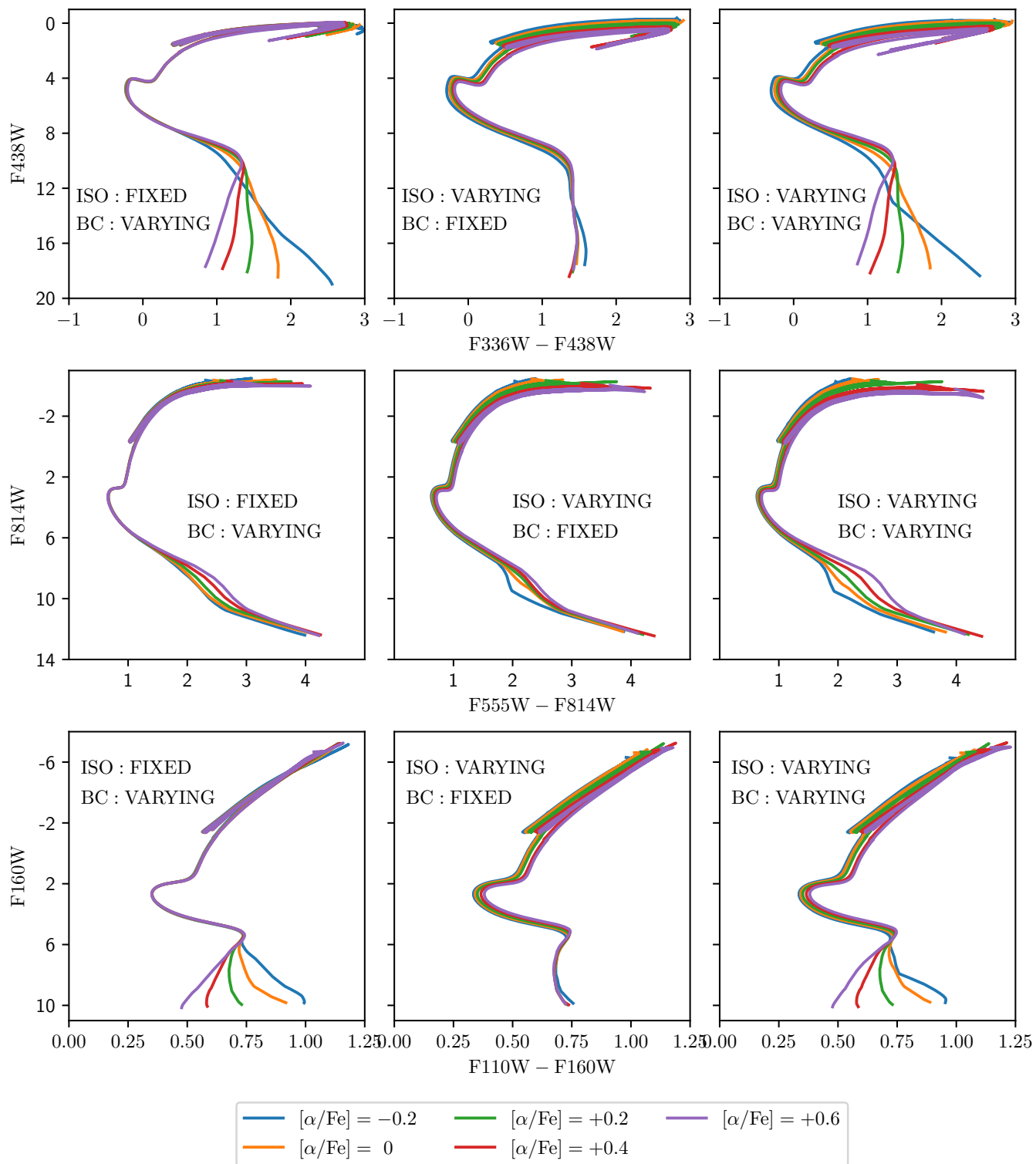


Figure 5. Isochrones at 8 Gyr and $[\text{Fe}/\text{H}] = -0.5$ for three different HST-WFC3 CMDs. The panels demonstrate the effect of varying $[\alpha/\text{Fe}]$ on the bolometric corrections and the underlying isochrones. The left column shows the effect of varying $[\alpha/\text{Fe}]$ in the BCs while keeping the underlying isochrone fixed at $[\alpha/\text{Fe}] = +0.2$. The middle panel shows the effect of varying $[\alpha/\text{Fe}]$ in the isochrones while leaving the BCs fixed at $[\alpha/\text{Fe}] = +0.2$. The right panel shows the combined effect of varying both components together.

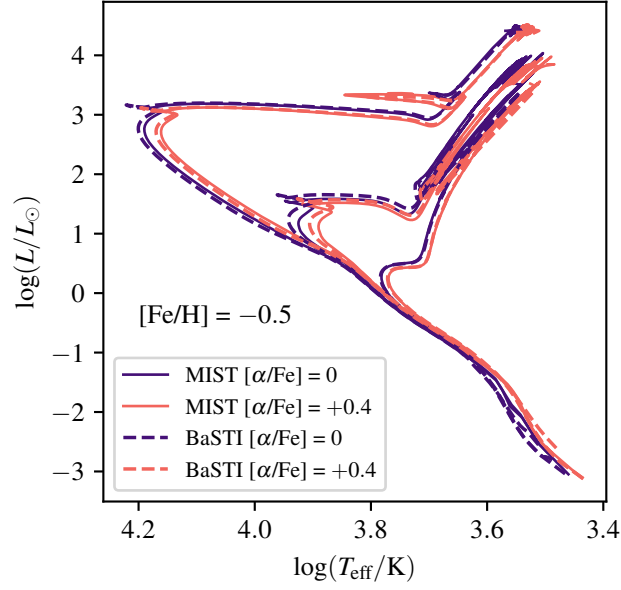


Figure 6. Isochrones at 100 Myr, 1 Gyr, and 10 Gyr from MIST (solid lines) and BaSTI (dashed lines). Darker colors show solar-scaled $[\alpha/\text{Fe}] = 0$ isochrones, while lighter colors show $[\alpha/\text{Fe}] = +0.4$ enhanced isochrones.

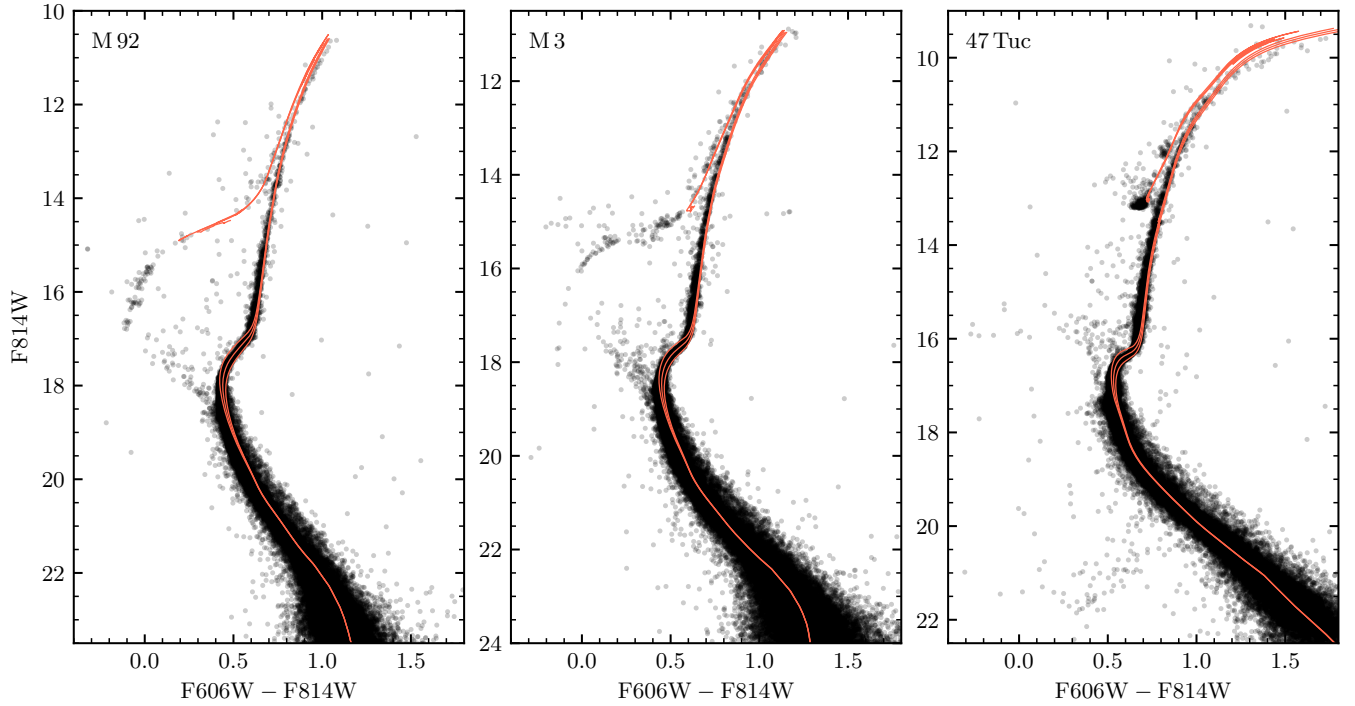


Figure 7. Comparison of metal-poor, α -enhanced isochrones with the HST/ACS CMDs of three Galactic globular clusters: M92 (left), M3 (center), and 47 Tuc (right). Four ages from 10 to 13 Gyr are shown; all have $[\alpha/\text{Fe}] = +0.4$. The data are from the ACS Survey of Galactic Globular Clusters (Sarajedini et al. 2007; Anderson et al. 2008). Model $[\text{Fe}/\text{H}]$, distance modulus, and reddening parameters are given in Table 2.

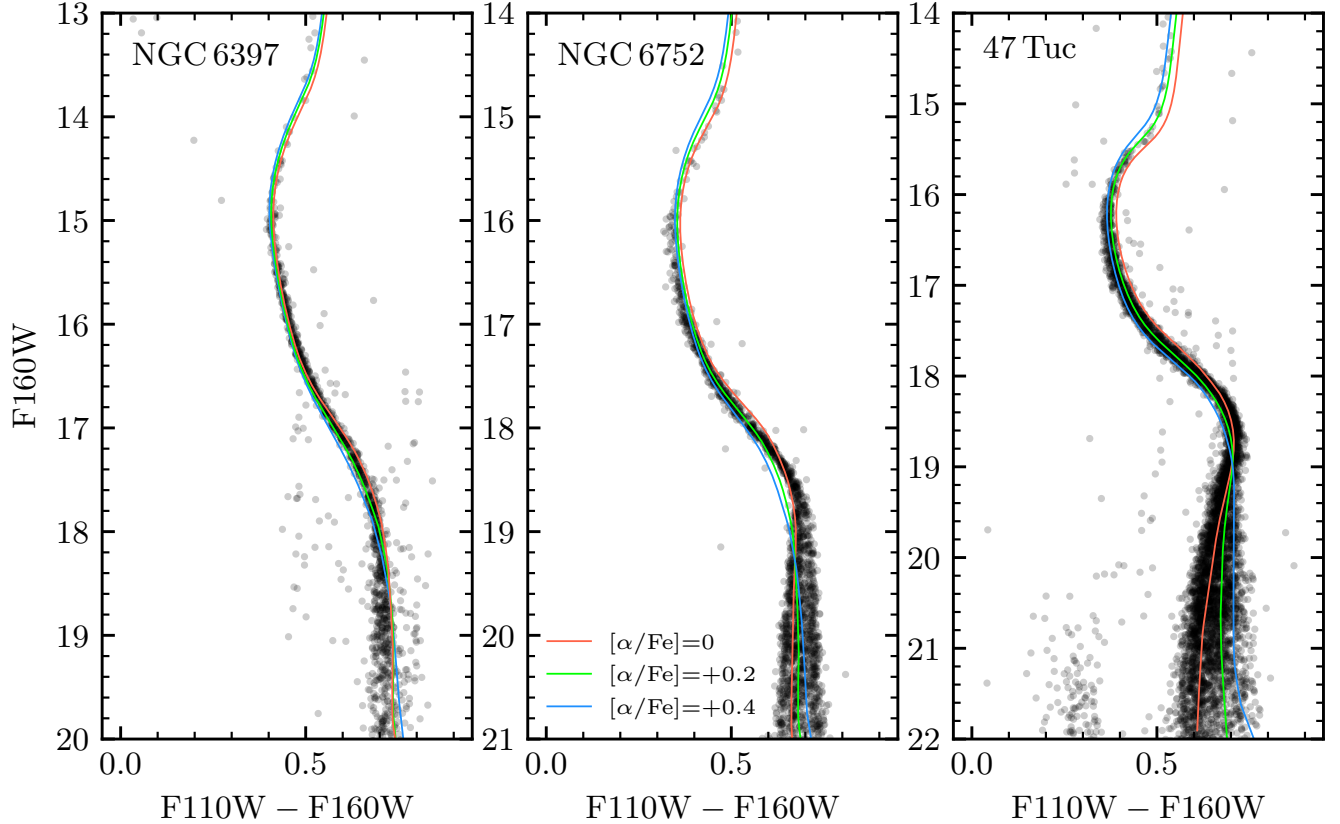


Figure 8. Comparison of metal-poor isochrones with the HST/WFC3 CMDs of three Galactic globular clusters: NGC 6397 (left), NGC 6752 (center), and 47 Tuc (right). In each panel, the observations are compared with models at a fixed $[\text{Fe}/\text{H}]$ and age but with three different values of $[\alpha/\text{Fe}]$. Model $[\text{Fe}/\text{H}]$, distance modulus, and reddening parameters are given in Table 2.

Table 2. Globular cluster and model parameters for Figures 7 and 8

Cluster	DM	$E(B-V)$	$[\text{Fe}/\text{H}]$
47 Tuc	13.266	0.04	-0.72
M 3	15.043	0.01	-1.50
M 92	14.595	0.02	-2.31
NGC 6497	11.920	0.18	-2.02
NGC 6752	13.010	0.04	-1.54

NOTE—Distance modulus (DM) and reddening ($E(B-V)$) from [Gaia Collaboration et al. \(2018\)](#); $[\text{Fe}/\text{H}]$ from the latest edition of the [Harris \(1996\)](#) catalog.

Figure 8 shows WFC3/IR photometry of NGC 6397 ([Milone & Marino 2022](#)), NGC 6752 ([Dondoglio et al. 2022](#)), and 47 Tuc ([Milone et al. 2025](#)). In contrast to Figure 7, we show only one age per panel (13 Gyr) but vary $[\alpha/\text{Fe}]$ to show the marked effect of varying the α -capture elements on the lower main sequence, as mentioned in §3.2. Again the parameters used for the figure are given in Table 2.

4. SUMMARY

The MIST isochrones have been updated and expanded to include the effects of α -enhancement. The α -enhanced grid covers the range of $-3 \leq [\text{Fe}/\text{H}] \leq +0.5$ and includes $[\alpha/\text{Fe}] = -0.2, 0, +0.2, +0.4, \text{ and } +0.6$ for all $[\text{Fe}/\text{H}]$ values, excepting $[\text{Fe}/\text{H}] = +0.5, [\alpha/\text{Fe}] = +0.6$ due to lack of input physics above $Z = 0.1$. Stellar evolution tracks and isochrones are provided from the MIST project webpage. The file formats are identical to those used in Paper 1.

A number of relatively minor changes to the physics used in MESA have been made but the resulting models have been validated with comparisons to models from Paper 1 and BaSTI as well as observations of Galactic globular clusters. The necessary tools to reproduce the models presented in this paper are made available via Zenodo;⁵ links to these repositories are included on the MIST project webpage.

1 The work presented in this paper would not have been possible without the tremendous contributions of Bill Paxton.
 2 Thanks to Bill and all of the MESA developers for creating and supporting MESA. AD received financial support from
 3 HST-AR-15793. Support for Program number HST-AR-15793 was provided by NASA through a grant from the
 4 Space Telescope Science Institute, which is operated by the Association of Universities for Research in Astronomy,
 5 Incorporated, under NASA contract NAS5-26555. AD also received financial support from the European Research
 6 Council (ERC) under the Horizon Europe programme (Synergy Grant agreement No. 101071505: 4D-STAR). This
 7 work is partially funded by the European Union. Views and opinions expressed are, however, those of the authors only
 8 and do not necessarily reflect those of the European Union or the European Research Council. The Flatiron Institute
 9 is supported by the Simons Foundation.

APPENDIX

Section 2.2 mentions that a few changes have been introduced into MESA revision 11701 for this paper. The purpose of this Appendix is to catalog the changes made to source code files. All files that are mentioned here, as well as all data and input files required to reproduce the models, are included in the Zenodo repositories (Dotter & Bauer 2025a,b). The changes are listed in no particular order.

- In SVN commit 13223 the mass of the proton (`mp`) was changed to the atomic mass unit (`amu`) at line number 283 in `mesa/eos/private/eospc_eval.f90`. The result of this change is to smooth out the transition between the PC and HELM equations of state.
- FreeEOS tables were imported from Jermyn et al. (2023). This required changing parameters in the file `mesa/eos/public/eos_def.f` related to the number of X and Z values supported by the EOS tables.
- The file `mesa/atm/private/table_atm.f90` was modified to take into account the $[\alpha/\text{Fe}]$ value listed in the table headers. The $[\alpha/\text{Fe}]$ value was included in the table header specification since Paxton et al. (2011) but was never utilized because all previous versions of the atmosphere boundary condition tables were only for scaled-solar composition. The atmosphere boundary condition tables used in this paper were calculated with α -enhanced chemical compositions.
- The file `mesa/star/private/turbulent_diffusion.f90` was modified to include the turbulent diffusion model described by Dotter et al. (2017).
- In SVN commit 11971 the file `mesa/star/private/element_diffusion.f90` was changed at lines 184-185 to fix a bug in identifying the location of a convection zone.

Software: MESA SDK (Townsend 2019), MESA rev. 11701 (Paxton 2019), iso (Dotter 2016b), matplotlib (Hunter 2007), numpy (Harris et al. 2020), Python (Van Rossum & Drake 2009)

⁵ <https://zenodo.org/records/15232687>, <https://zenodo.org/records/15213406>

REFERENCES

- Anderson, J., Sarajedini, A., Bedin, L. R., et al. 2008, *AJ*, 135, 2055
- Asplund, M., Grevesse, N., Sauval, A. J., & Scott, P. 2009, *ARA&A*, 47, 481
- Basu, S., Mazumdar, A., Antia, H. M., & Demarque, P. 2004, *MNRAS*, 350, 277
- Bauer, E. B. 2023, *ApJ*, 950, 115
- Bensby, T., Feltzing, S., & Oey, M. S. 2014, *A&A*, 562, A71
- Bessell, M., & Murphy, S. 2012, *PASP*, 124, 140
- Bohlin, R. C. 2016, *AJ*, 152, 60
- Bressan, A., Marigo, P., Girardi, L., et al. 2012, *MNRAS*, 427, 127
- Caffau, E., Ludwig, H.-G., Steffen, M., Freytag, B., & Bonifacio, P. 2011, *SoPh*, 268, 255
- Chabrier, G., & Baraffe, I. 1997, *A&A*, 327, 1039
- Chen, Y., Girardi, L., Bressan, A., et al. 2014, *MNRAS*, 444, 2525
- Choi, J., Dotter, A., Conroy, C., et al. 2016, *ApJ*, 823, 102
- Clayton, D. D. 1984, *Principles of stellar evolution and nucleosynthesis*.
- Conroy, C. 2013, *ARA&A*, 51, 393
- Cullen, F., McLure, R. J., Dunlop, J. S., et al. 2019, *MNRAS*, 487, 2038
- Cyburt, R. H., Amthor, A. M., Ferguson, R., et al. 2010, *The Astrophysical Journal Supplement Series*, 189, 240. <https://doi.org/10.1088/0067-0049/189/1/240>
- Deheuvels, S., Ballot, J., Beck, P. G., et al. 2015, *A&A*, 580, A96
- Dondoglio, E., Milone, A. P., Renzini, A., et al. 2022, *ApJ*, 927, 207
- Dotter, A. 2016a, *ApJS*, 222, 8
- . 2016b, *ISO: Isochrone construction*, *Astrophysics Source Code Library*, record ascl:1601.021, ,
- . 2022, *Research Notes of the American Astronomical Society*, 6, 112
- Dotter, A., & Bauer, E. 2025a, *MESA for MIST*, vr11701-modified, *Zenodo*, doi:10.5281/zenodo.15213405. <https://doi.org/10.5281/zenodo.15213405>
- . 2025b, *MESA Work Directories, v1*, *Zenodo*, doi:10.5281/zenodo.15232686. <https://doi.org/10.5281/zenodo.15232686>
- Dotter, A., Chaboyer, B., Ferguson, J. W., et al. 2007a, *ApJ*, 666, 403
- . 2007b, *ApJ*, 666, 403
- Dotter, A., Chaboyer, B., Jevremović, D., et al. 2008, *ApJS*, 178, 89
- Dotter, A., Conroy, C., Cargile, P., & Asplund, M. 2017, *ApJ*, 840, 99
- Dotter, A., Ferguson, J. W., Conroy, C., et al. 2015, *MNRAS*, 446, 1641
- Espinosa Lara, F., & Rieutord, M. 2011, *A&A*, 533, A43
- Ferguson, J. W., Alexander, D. R., Allard, F., et al. 2005, *ApJ*, 623, 585
- Fitzpatrick, E. L., & Massa, D. 2007, *ApJ*, 663, 320
- Fu, X., Bressan, A., Marigo, P., et al. 2018, *MNRAS*, 476, 496
- Fuller, J., Piro, A. L., & Jermyn, A. S. 2019, *MNRAS*, 485, 3661
- Gaia Collaboration, Babusiaux, C., van Leeuwen, F., et al. 2018, *A&A*, 616, A10. <https://doi.org/10.1051/0004-6361/201832843>
- Gehan, C., Mosser, B., Michel, E., Samadi, R., & Kallinger, T. 2018, *A&A*, 616, A24
- Girardi, L., Dalcanton, J., Williams, B., et al. 2008, *PASP*, 120, 583
- Grevesse, N., & Sauval, A. J. 1998, *SSRv*, 85, 161
- Harris, C. R., Millman, K. J., van der Walt, S. J., et al. 2020, *Nature*, 585, 357. <https://doi.org/10.1038/s41586-020-2649-2>
- Harris, W. E. 1996, *AJ*, 112, 1487
- Heger, A., Langer, N., & Woosley, S. E. 2000, *ApJ*, 528, 368
- Hermes, J. J., Gänsicke, B. T., Kawaler, S. D., et al. 2017, *ApJS*, 232, 23
- Herwig, F. 2000, *A&A*, 360, 952
- Hidalgo, S. L., Pietrinferni, A., Cassisi, S., et al. 2018, *ApJ*, 856, 125
- Hunter, J. D. 2007, *Computing in Science & Engineering*, 9, 90
- Iglesias, C. A., & Rogers, F. J. 1996, *ApJ*, 464, 943
- Jermyn, A. S., Bauer, E. B., Schwab, J., et al. 2023, *ApJS*, 265, 15
- Joyce, M., Molnár, L., Cinquegrana, G., et al. 2024, *ApJ*, 971, 186
- Kashino, D., Lilly, S. J., Renzini, A., et al. 2022, *ApJ*, 925, 82
- Koornneef, J., Bohlin, R., Buser, R., Horne, K., & Turnshek, D. 1986, *Highlights of Astronomy*, 7, 833
- Kopal, Z. 1978, *Dynamics of close binary systems*, doi:10.1007/978-94-009-9780-6
- Kurucz, R. L. 1970, *SAO Special Report*, 309
- . 1993, *SYNTHE spectrum synthesis programs and line data*
- . 2011, *Canadian Journal of Physics*, 89, 417
- Kurucz, R. L., & Avrett, E. H. 1981, *SAO Special Report*, 391
- Magg, E., Bergemann, M., Serenelli, A., et al. 2022, *A&A*, 661, A140

- Mamajek, E. E., Torres, G., Prsa, A., et al. 2015, arXiv e-prints, arXiv:1510.06262
- Marigo, P., Bressan, A., Nanni, A., Girardi, L., & Pumo, M. L. 2013, *MNRAS*, 434, 488
- Marigo, P., Girardi, L., Bressan, A., et al. 2017, *ApJ*, 835, 77
- McKemmish, L. K., Masseron, T., Hoeijmakers, H. J., et al. 2019, *MNRAS*, 488, 2836
- Milone, A. P., & Marino, A. F. 2022, *Universe*, 8, 359
- Milone, A. P., Marino, A. F., Bernizzoni, M., et al. 2025, *A&A*, 698, A247
- Morel, P., & Thévenin, F. 2002, *A&A*, 390, 611
- Mosser, B., Goupil, M. J., Belkacem, K., et al. 2012, *A&A*, 548, A10
- Nataf, D. M., Gould, A. P., Pinsonneault, M. H., & Udalski, A. 2013, *ApJ*, 766, 77
- Nguyen, C. T., Costa, G., Girardi, L., et al. 2022, *A&A*, 665, A126
- Oke, J. B. 1974, *ApJS*, 27, 21
- Oke, J. B., & Schwarzschild, M. 1952, *ApJ*, 116, 317
- Paxton, B. 2019, *Modules for Experiments in Stellar Astrophysics (MESA)*, vr11701, Zenodo, doi:10.5281/zenodo.2665077. <https://doi.org/10.5281/zenodo.2665077>
- Paxton, B., Bildsten, L., Dotter, A., et al. 2011, *ApJS*, 192, 3
- Paxton, B., Cantiello, M., Arras, P., et al. 2013, *ApJS*, 208, 4
- Paxton, B., Marchant, P., Schwab, J., et al. 2015, *ApJS*, 220, 15
- Paxton, B., Schwab, J., Bauer, E. B., et al. 2018, *ApJS*, 234, 34
- Paxton, B., Smolec, R., Schwab, J., et al. 2019, *ApJS*, 243, 10
- Pietrinferni, A., Cassisi, S., Salaris, M., & Castelli, F. 2006, *ApJ*, 642, 797
- Pietrinferni, A., Hidalgo, S., Cassisi, S., et al. 2021, *ApJ*, 908, 102
- Pietrow, A. G. M., Hoppe, R., Bergemann, M., & Calvo, F. 2023, *A&A*, 672, L6
- Pinsonneault, M. H., Kawaler, S. D., Sofia, S., & Demarque, P. 1989, *ApJ*, 338, 424
- Planck Collaboration, Ade, P. A. R., Aghanim, N., et al. 2015, ArXiv:1502.01589, arXiv:1502.01589
- Potekhin, A. Y., & Chabrier, G. 2010, *Contributions to Plasma Physics*, 50, 82
- Pritzl, B. J., Venn, K. A., & Irwin, M. 2005, *AJ*, 130, 2140
- Prša, A., Harmanec, P., Torres, G., et al. 2016, *AJ*, 152, 41
- Rogers, F. J., & Nayfonov, A. 2002, *ApJ*, 576, 1064
- Salaris, M., Chieffi, A., & Straniero, O. 1993, *ApJ*, 414, 580
- Salaris, M., & Weiss, A. 1998, *A&A*, 335, 943
- Salasnich, B., Girardi, L., Weiss, A., & Chiosi, C. 2000, *A&A*, 361, 1023
- Sarajedini, A., et al. 2007, *AJ*, 133, 1658
- Saumon, D., Chabrier, G., & van Horn, H. M. 1995, *ApJS*, 99, 713
- Sbordone, L., Salaris, M., Weiss, A., & Cassisi, S. 2011, *A&A*, 534, A9
- Spruit, H. C. 2002, *A&A*, 381, 923
- Steidel, C. C., Strom, A. L., Pettini, M., et al. 2016, *ApJ*, 826, 159
- Timmes, F. X., & Swesty, F. D. 2000, *ApJS*, 126, 501
- Tolstoy, E., Hill, V., & Tosi, M. 2009, *ARA&A*, 47, 371
- Topping, M. W., Shapley, A. E., Reddy, N. A., et al. 2020, *MNRAS*, 499, 1652
- Townsend, R. 2019, *MESA SDK for Linux*, v20190503, Zenodo, doi:10.5281/zenodo.2669541. <https://doi.org/10.5281/zenodo.2669541>
- Trager, S. C., Faber, S. M., Worthey, G., & González, J. J. 2000, *AJ*, 119, 1645
- Van Rossum, G., & Drake, F. L. 2009, *Python 3 Reference Manual* (Scotts Valley, CA: CreateSpace)
- VandenBerg, D. A., Bergbusch, P. A., Dotter, A., et al. 2012, *ApJ*, 755, 15
- VandenBerg, D. A., Bergbusch, P. A., Ferguson, J. W., & Edvardsson, B. 2014, *ApJ*, 794, 72
- Vernazza, J. E., Avrett, E. H., & Loeser, R. 1981, *ApJS*, 45, 635
- Weiss, A., Salaris, M., Ferguson, J. W., & Alexander, D. R. 2006, arXiv e-prints, astro
- Worthey, G. 1994, *ApJS*, 95, 107
- Worthey, G., Faber, S. M., & Gonzalez, J. J. 1992, *ApJ*, 398, 69